

Exceptional Cocatalyst-Free Photo-Enhanced Piezocatalytic Hydrogen Evolution of Carbon Nitride Nanosheets from Strong In-Plane Polarization

HPSTAR
1291-2021

Cheng Hu, Fang Chen, Yonggang Wang, Na Tian,* Tianyi Ma, Yihe Zhang, and Hongwei Huang*

Utilizing mechanical energy to produce hydrogen is emerging as a promising way to generate renewable energy, but is challenged by low efficiency and scanty cognition. In this work, graphitic carbon nitride ($g\text{-C}_3\text{N}_4$) with an atomically thin sheet-like structure is applied for prominent piezocatalytic and photo-enhanced piezocatalytic H_2 production. It is revealed that the anomalous piezoelectricity in $g\text{-C}_3\text{N}_4$ originates from the strong in-plane polarization along the a -axis, contributed by the superimposed polar tri-s-triazine units and flexoelectric effect derived from the structured triangular cavities, which provides powerful electrochemical driving force for the water reduction reaction. Furthermore, the photo-enhanced charge transfer enables $g\text{-C}_3\text{N}_4$ nanosheets to reserve more energized polarization charges to fully participate in the reaction at the surface reactive sites enriched by strain-induced carbon vacancies. Without any cocatalysts, an exceptional photo-piezocatalytic H_2 evolution rate of $12.16 \text{ mmol g}^{-1} \text{ h}^{-1}$ is delivered by the $g\text{-C}_3\text{N}_4$ nanosheets, far exceeding that of previously reported piezocatalysts and $g\text{-C}_3\text{N}_4$ photocatalysts. Further, high pure-water-splitting performance with production of the value-added oxidation product H_2O_2 via photo-piezocatalysis is also disclosed. This work not only exposes the potential of $g\text{-C}_3\text{N}_4$ as a piezo-semiconductor for catalytic H_2 evolution, but also breaks a new ground for the conversion of solar and mechanical energy by photomediated piezocatalytic reaction.

1. Introduction

The massive energy consumption and aggravated environmental pollution compel us to exploit clean renewable energy resources to replace traditional fossil fuels, and hydrogen with the high energy density (142 MJ kg^{-1}) has become a research hotspot in the energy field.^[1–4] Recent research has shown that piezocatalytic water splitting is a promising and environmentally friendly way to produce H_2 via a mechanical-to-chemical energy-conversion process.^[5] The piezoelectric potential resulted from the variation of polarization state upon strain can generate an energy shift on the occupied and unoccupied electronic states in the whole crystal with noncentrosymmetric (NCS) crystal structure. The discontinuity of occupied electronic states between the piezoelectric and electroactive species in water provides a driving force for electron transfer at the solid-liquid interface, and thus induces the water-splitting reaction directly.^[6,7] Moreover, the strain-induced piezoelectric field can also modulate the


carrier migration in bulk and on the surface of piezoelectrics, as well as the band bending at the interface of heterojunction, which further improve the catalytic activity of piezo-semiconductors for H_2 production based on the piezo-phototronic effect.^[8,9] Nevertheless, most of the semiconducting piezoelectrics suffer from small mechanical energy capture area, weak piezoelectric polarization and insufficient catalytic active sites, which severely limit their practical applications.

Atomically thin 2D piezoelectric materials possess high piezoelectric coefficient, large specific surface area and high surface atom ratio, which have been regarded as the ideal piezocatalysts to break the abovementioned restrictions.^[10–13] For instance, atomically thin ZnS nanosheets with a typical piezoelectric wurtzite structure showed a superior piezocatalytic H_2 production rate of $1.08 \text{ mmol g}^{-1} \text{ h}^{-1}$, which benefits from the large piezo-potential, efficient energy harvesting and rich reactive sites.^[14] Some transition metal dichalcogenides crystallize in centrosymmetric (CS) structure and are nonpolar, but their uniform odd atomic layers have the strong piezoelectric

C. Hu, F. Chen, Dr. N. Tian, Prof. Y. H. Zhang, Prof. H. W. Huang
Beijing Key Laboratory of Materials Utilization of Nonmetallic Minerals and Solid Wastes
National Laboratory of Mineral Materials
School of Materials Science and Technology
China University of Geosciences
Beijing 100083, China
E-mail: tianna65@cugb.edu.cn; hhw@cugb.edu.cn

Dr. Y. G. Wang
Center for High Pressure Science and Technology Advanced Research (HPSTAR)
Beijing 100094, China

Dr. T. Y. Ma
Centre for Translational Atomaterials
Swinburne University of Technology
Hawthorn, Victoria 3122, Australia

 The ORCID identification number(s) for the author(s) of this article can be found under <https://doi.org/10.1002/adma.202101751>.

DOI: 10.1002/adma.202101751

polarization.^[15] Wang et al. reported that the few-layers MoS₂ modified by glutathione exhibited high water-splitting performance with a H₂ evolution rate of ≈1.25 mmol g⁻¹ h⁻¹ under ultrasonic vibration. The piezoelectric field along the [001] direction and abundant edge active sites facilitate the charge transport and reaction kinetics.^[16] Except for these intrinsic polar planes with piezoelectricity, the asymmetric atom arrangement and charge density distribution can be created in graphene, which is inherently nonpiezoelectric and conductive, by introducing polar groups or nanoscale triangular-shaped holes. Zhang et al. fabricated an electrocatalytic nanocomposite composed of the N-doped graphene vesicles and MoC quantum dots, where the doped graphene provided enough piezoelectric potential to trigger H₂ evolution reactions under ultrasonic irradiation. The high H₂ evolution rate (≈1.69 mmol g⁻¹ h⁻¹) indicates that the functionalized graphene is an excellent candidate for piezocatalytic H₂ production.^[17] Though encouraging progress has been made, exploiting new 2D piezocatalyst system for more efficient mechanical-energy triggered H₂ evolution is highly challenging.

Graphitic carbon nitride (g-C₃N₄) is a very promising and widely studied semiconductor photocatalyst for H₂ evolution due to its moderate bandgap (≈2.7 eV), favorable band edge potentials, superior physicochemical stability and facile preparation procedure.^[18,19] Although the bulk g-C₃N₄ has a CS crystal structure, intriguingly g-C₃N₄ has uniformly distributed triangular nanopores in its tri-s-triazine layers, which results in the strong flexoelectricity and in-plane piezoelectricity in tri-s-triazine plane.^[20] Encouraged by the analogous structure to graphite, g-C₃N₄ can be exfoliated into monolayer or few-layers as a result of the weak interplanar van der Waals interaction. The piezoelectric coefficient of g-C₃N₄ nanosheet has been determined as 0.732 C m⁻², much higher than that of the quartz and h-BN that extensively applied to nanoelectromechanical systems.^[21] It is worth mentioning that the piezoelectricity still retains in the bulk phase of g-C₃N₄ due to the distinctive atomic stacking structure, which is unlike MoS₂ and WS₂ whose piezocatalytic efficiency is dramatically reduced in the even atomic layers.^[22] Combining with the plentiful hydrogen bonds between chains of polymeric melon units promoting the adsorption and activation of H₂O molecules, it can be speculated that g-C₃N₄ 2D nanosheets may be an ideal material to harvest mechanical energy to produce H₂. It has been demonstrated that the bulk g-C₃N₄ is capable of generating H₂O₂ through the piezocatalytic process, which also encourages us to investigate the piezocatalytic H₂ evolution performance of g-C₃N₄ nanosheets.^[23] Particularly, in view of the excellent semiconducting characteristics of g-C₃N₄, it is attractive to explore the light-mediated piezocatalytic H₂ evolution activity and the intrinsic mechanism.

In this work, ultrathin g-C₃N₄ nanosheets are synthesized by thermal oxidation etching of bulk g-C₃N₄ under air followed by ultrasonic exfoliation. Piezoresponse force microscopy (PFM) revealed that g-C₃N₄ nanosheets show stronger piezoelectricity than the bulk counterpart. The origin of the anomalous piezoelectricity of g-C₃N₄ nanosheets is elucidated by the finite element method (FEM) and density functional theory (DFT) at atomic level. Under simultaneous light and ultrasonic irradiation without cocatalyst, ultrathin g-C₃N₄ nanosheets

display a superb photo-piezocatalytic H₂ evolution rate of 12.16 mmol g⁻¹ h⁻¹, which is much higher than bulk g-C₃N₄, also surpassing that under sole ultrasonic irradiation. The surface potential and charge conduction characteristics of the two piezocatalysts are investigated by the photo-assisted Kelvin probe force microscopy (KPFM) and piezoelectrochemical measurements respectively to explicate the activity reinforcement mechanism. Moreover, the surface structures and reactive sites of catalysts are also studied by in situ high-pressure Raman spectroscopy and metal deposition with different excitation sources to get an in-depth understanding on the reaction process.

2. Results and Discussion

2.1. Catalysts Characterization

Ultrathin g-C₃N₄ nanosheets (UT-g-C₃N₄) are prepared via direct thermal oxidation etching of bulk g-C₃N₄ under air atmosphere, followed by ultrasonic exfoliation to obtain uniformly dispersed nanosheets (Figure 1a). As the in-planar hydrogen bond cohering chains of polymeric tri-s-triazine units in the layers are not stable enough to against the oxidation effect exerted by O₂ at high temperature, the weak van der Waals force between layers can be overcome to exfoliate bulk g-C₃N₄ into monolayer or few-layers.^[24] It can be seen that the as-obtained g-C₃N₄ nanosheets become fluffy, and the volume is much larger than that of the bulk counterpart with the same weight, indicating the decreased thickness of UT-g-C₃N₄ (Figure S1, Supporting Information). Transmission electron microscopy (TEM) and scanning electron microscopy (SEM) images show that the UT-g-C₃N₄ possesses an ultrathin sheet-like morphology, while the bulk g-C₃N₄ products are composed of blocks stacked by numerous layers with size of several micrometers (Figure 1b, Figure S2, Supporting Information). Atomic force microscopy (AFM) demonstrates that even the flake stripped from bulk g-C₃N₄ still has a thickness of ≈25 nm, while the thickness of g-C₃N₄ nanosheets decreases to ≈1.5–2 nm, which comprise four or five atomic layers (Figure 1c). The ultrathin sheet-like structure of UT-g-C₃N₄ is expected to strengthen the mechanical energy harvesting, which can generate a higher piezo-potential for electrochemical redox reactions.

The microstructure change from bulk g-C₃N₄ to UT-g-C₃N₄ is further revealed by the X-ray diffraction (XRD) pattern and Raman spectra. As shown in Figure 1e, bulk g-C₃N₄ exhibits a typical XRD pattern with two pronounced characteristic peaks, namely the (100) peak at 13.1° representing in-planar tri-s-triazine repeating packing and (002) peak at 27.4° originated from the interlayer stacking.^[25] In contrast, the intensity of both peaks is weakened in UT-g-C₃N₄, demonstrating the reduced thickness and size of nanosheets after thermal oxidation etching and ultrasonic exfoliation. Besides, the (002) peak of UT-g-C₃N₄ shifts from 27.4° to 27.6° compared to bulk g-C₃N₄, which indicates a decreased interlayer stacking distance in the nanosheets. The Raman characteristic peaks of UT-g-C₃N₄ and bulk g-C₃N₄ from 478 to 1568 cm⁻¹ are indexed to the vibration modes of CN heterocycles. The bands at 705 and 979 cm⁻¹ are ascribed to the

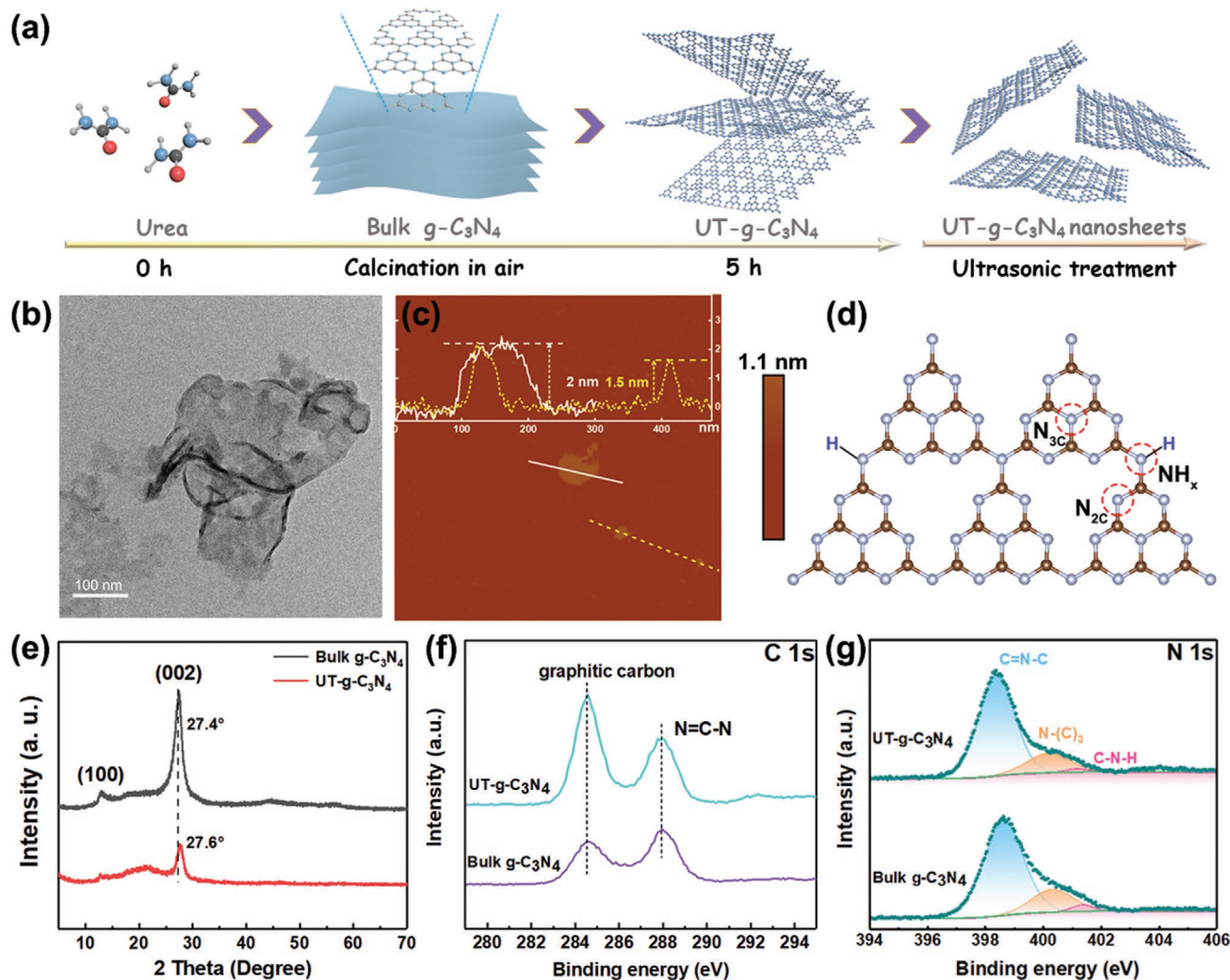


Figure 1. a) Schematic preparation process of ultrathin $g\text{-C}_3\text{N}_4$ nanosheets. b) TEM, c) AFM images and the corresponding height curve (inset) of UT- $g\text{-C}_3\text{N}_4$. d) The diagram of different N sites in the tri-s-triazine layer. e) XRD patterns, and f, g) XPS C 1s (f) and N 1s (g) spectra of UT- $g\text{-C}_3\text{N}_4$ and bulk $g\text{-C}_3\text{N}_4$.

ring breathing modes of s-triazine in the crystal structure, and the peak at around 1568 cm^{-1} reflects the stretching vibration of melem units.^[26] All these peaks show remarkable decrease in intensity, confirming the formation of ultrathin structure in UT- $g\text{-C}_3\text{N}_4$ (Figure S3, Supporting Information).

X-ray photoelectron spectroscopy (XPS) is recorded to examine the chemical states and bonding structures of samples. There are no obvious binding energy shifts of the C 1s and N 1s peaks, indicating that the same chemical states exist in both UT- $g\text{-C}_3\text{N}_4$ and bulk $g\text{-C}_3\text{N}_4$. The two peaks with binding energies of 284.6 and 288.0 eV in the C 1s spectrum basically correspond to graphitic carbon (C=C) and sp^2 -bonded carbon (N=C-N), respectively (Figure 1f). The decreased peak area ratio of N=C-N to C=C in UT- $g\text{-C}_3\text{N}_4$ is mainly attributed to the decomposition of partial melems in the layers during oxidation etching process.^[27] In the N 1s spectrum, three sub-peaks centering at 398.6, 400.3 and 401.4 eV are assigned to the sp^2 -hybridized nitrogen (C-N=C), N-(C)₃ and amino groups (C-N-H), respectively (Figure 1g). The

peak area ratio of N-(C)₃ to C-N-H in UT- $g\text{-C}_3\text{N}_4$ and bulk $g\text{-C}_3\text{N}_4$ is calculated to be 4.6 and 3.4, respectively. According to the structural model of the three N-linked bonds shown in Figure 1d, the increased N-(C)₃ to C-N-H area ratio in UT- $g\text{-C}_3\text{N}_4$ implies that it possesses more bonded tri-s-triazine units that are orderly arranged in the layers than the bulk counterpart, which serve as polar groups to produce higher in-plane piezoelectricity.

The optical properties and band structures of UT- $g\text{-C}_3\text{N}_4$ and bulk $g\text{-C}_3\text{N}_4$ are surveyed (Figure S4, Supporting Information). UV-vis diffuse reflectance spectra (DRS) exhibit a notable blue shift of the intrinsic absorption edge in UT- $g\text{-C}_3\text{N}_4$ with respect to bulk $g\text{-C}_3\text{N}_4$, which is attributed to the ultrathin structure induced quantum confinement effect separating the conduction band (CB) and valence band (VB) in opposite directions. The bandgap of UT- $g\text{-C}_3\text{N}_4$ and bulk $g\text{-C}_3\text{N}_4$ is determined to be 2.94 and 2.62 eV based on the Kubelka-Munk method.^[28] The positive slope of Mott-Schottky plots reveals the n-type semiconductor characteristics for both samples. As

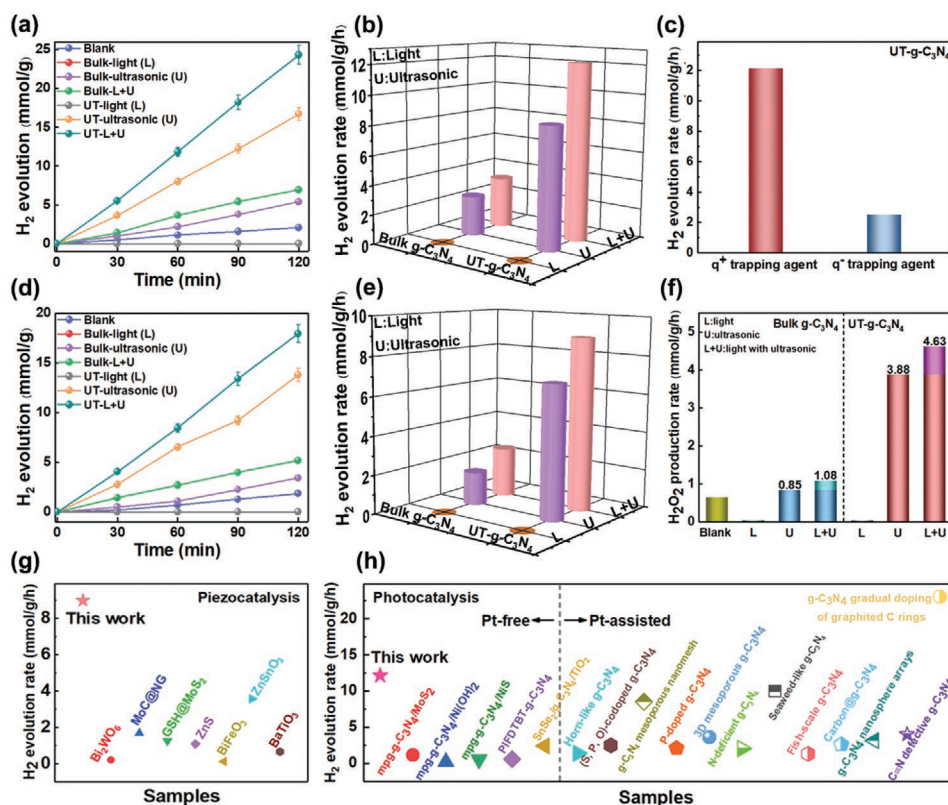


Figure 2. a) The H₂ yields and b) production rates of bulk g-C₃N₄ and UT-g-C₃N₄ under light, ultrasound, and simultaneous light and ultrasonic irradiation in glucose solution. c) The H₂ production rate of UT-g-C₃N₄ with different trapping agents in the photo-piezocatalytic process. d) The H₂ yields and e) production rates of bulk g-C₃N₄ and UT-g-C₃N₄ under light, ultrasound, and simultaneous light and ultrasonic irradiation in pure water. f) The H₂O₂ production rate of bulk g-C₃N₄ and UT-g-C₃N₄ under different conditions. g, h) H₂ evolution performance comparison of UT-g-C₃N₄ with the reported piezocatalysts (g) and g-C₃N₄-based photocatalysts (h). [14,16,17,29–49]

a result, the band structures of UT-g-C₃N₄ and bulk g-C₃N₄ are depicted, which well satisfy the thermodynamic requirement for H₂O reduction. Compared with the bulk sample, the more negative CB position in UT-g-C₃N₄ provides a larger thermodynamic driving force for electrochemical H₂ evolution.

2.2. Piezocatalytic and Photo-Piezocatalytic Hydrogen Evolution

The piezocatalytic and photo-piezocatalytic H₂ production are first conducted on g-C₃N₄ nanosheets with the addition of glucose as sacrificial agent in the absence of any cocatalysts. As shown in Figure 2a and b, UT-g-C₃N₄ and bulk g-C₃N₄ can hardly produce H₂ under light irradiation. When ultrasonic irradiation is applied, H₂ production occurs on both samples, and the H₂ evolution rate of UT-g-C₃N₄ and bulk g-C₃N₄ is 8.35 and 2.69 mmol g⁻¹ h⁻¹, respectively. The higher H₂ production of UT-g-C₃N₄ may be due to its larger piezoelectricity and more efficient vibration energy harvesting. Then, visible light ($\lambda \geq 420$ nm) is introduced into the ultrasonic reaction system, which results in further increased H₂ evolution for both samples. Under simultaneous irradiation by light and ultrasound, UT-g-C₃N₄ exhibits a prominent H₂ production rate of 12.16 mmol g⁻¹ h⁻¹, which is 3.5 times that of bulk g-C₃N₄. It is the highest value among the reported piezocatalysts for H₂

evolution, and even higher than that of the most g-C₃N₄-based photocatalysts assisted with Pt (Figure 2g, h). The improved photo-piezocatalytic performance suggests the significant role of illumination in promoting the piezocatalytic activity. Charge trapping experiments uncover that the photo-piezocatalytic performance of UT-g-C₃N₄ is remarkably suppressed with the addition of AgNO₃ as the negative charge (q⁻) trapping agent, demonstrating the piezoelectrically induced q⁻ is the main active species for generating H₂ during the photo-piezocatalytic process (Figure 2c). Besides, the crystalline phase of catalysts is kept unchanged after reactions, illustrating the high stability of catalysts (Figure S5, Supporting Information).

Subsequently, the pure-water-splitting experiment over bulk g-C₃N₄ and UT-g-C₃N₄ is also attempted under different conditions. The H₂ production is still only observed with ultrasound-involved irradiation, and the combined irradiation leads to the higher H₂ evolution activity for both samples. The highest H₂ production rate of 8.97 mmol g⁻¹ h⁻¹ is delivered by UT-g-C₃N₄ under light and ultrasound, which increases three-fold than bulk g-C₃N₄, about an enhancement more than 30% compared to that under ultrasound alone (Figure 2d,e). In this water-splitting process, the oxidation product of H₂O is also investigated. It is noteworthy that the oxidation product is value-added H₂O₂, illustrating that the piezo-potential induced positive charge (q⁺) oxidized OH⁻ to H₂O₂ instead of O₂. The

trend in H_2O_2 evolution over UT- $\text{g-C}_3\text{N}_4$ and bulk $\text{g-C}_3\text{N}_4$ under different irradiation conditions is highly consistent that in H_2 production. The highest H_2O_2 evolution rate obtained for UT- $\text{g-C}_3\text{N}_4$ under light and ultrasound is $4.63 \text{ mmol g}^{-1} \text{ h}^{-1}$, which is 4.3 times that of bulk $\text{g-C}_3\text{N}_4$ under same condition ($1.08 \text{ mmol g}^{-1} \text{ h}^{-1}$) (Figure 2f). To further figure out the possible reaction pathways of piezocatalytic pure water splitting, hydroxyl radicals ($\cdot\text{OH}$) are detected by the terephthalic acid photoluminescence (TA-PL) method.^[28] The strong PL peak at 425 nm indicates that UT- $\text{g-C}_3\text{N}_4$ generates a large amount of $\cdot\text{OH}$ when ultrasound is applied, and the introduction of visible light further facilitates the formation of $\cdot\text{OH}$. Based on the above analysis, the pure-water-splitting pathway can be presented as follows: first, the H_2O molecules are dissociated into H^+ and OH^- . For the reductive reaction, the piezoelectrically induced q^- reduces the H^+ to H_2 with a two-electron transfer process. In the oxidative reaction, the OH^- is oxidized by q^+ to form $\cdot\text{OH}$, and two $\cdot\text{OH}$ combine to form H_2O_2 (Figure S6, Supporting Information). However, it can be obviously seen that the molar ratio of produced H_2 and H_2O_2 is not 1:1, which may result from the incomplete $\cdot\text{OH}$ conversion and two-step reactions of water oxidation decreasing the H_2O_2 production rate. Due to the high catalytic performance with yielding the value-added H_2 and H_2O_2 , the photo-piezocatalysis of ultrathin $\text{g-C}_3\text{N}_4$ nanosheets holds a great potential for practical applications.

2.3. Piezoelectricity and In-Plane Polarization of $\text{g-C}_3\text{N}_4$

The anomalous piezoelectricity in bulk $\text{g-C}_3\text{N}_4$ and UT- $\text{g-C}_3\text{N}_4$ is investigated by PFM. As shown in Figure 3a, a distinct resonant peak near 286 kHz reflects the piezoelectric vibration excited by voltage in $\text{g-C}_3\text{N}_4$. The amplitude exhibits a significant correlation with the excitation voltage, confirming the linear piezoelectricity of the $\text{g-C}_3\text{N}_4$ (Figure 3b). The phase mapping well matches with the morphology, which suggests the uniform distribution of polarization in the bulk and nanosheets. Moreover, the relatively strong piezoelectricity is further confirmed by the butterfly amplitude loop and phase curve, where the maximum effective piezoelectric coefficient of UT- $\text{g-C}_3\text{N}_4$ and bulk $\text{g-C}_3\text{N}_4$ is determined as ≈ 524 and 392 pm V^{-1} , respectively (Figure 3c, Figure S7, Supporting Information), revealing that fabrication of ultrathin structure in $\text{g-C}_3\text{N}_4$ causes a larger piezoelectricity. The excellent piezoelectricity of $\text{g-C}_3\text{N}_4$ nanosheets can produce more polarization charges with the applied external stress, facilitating the surface redox reactions efficiently.

Piezoelectric polarization can be produced from the displacement of positive and negative charge centers in the asymmetric unit cell or by the strain gradient induced flexoelectric effect in dielectrics. To probe the origin of polarization in $\text{g-C}_3\text{N}_4$, the unit-cell dipole moment of $\text{g-C}_3\text{N}_4$ crystal models with different numbers of tri-s-triazine units along the a -axis

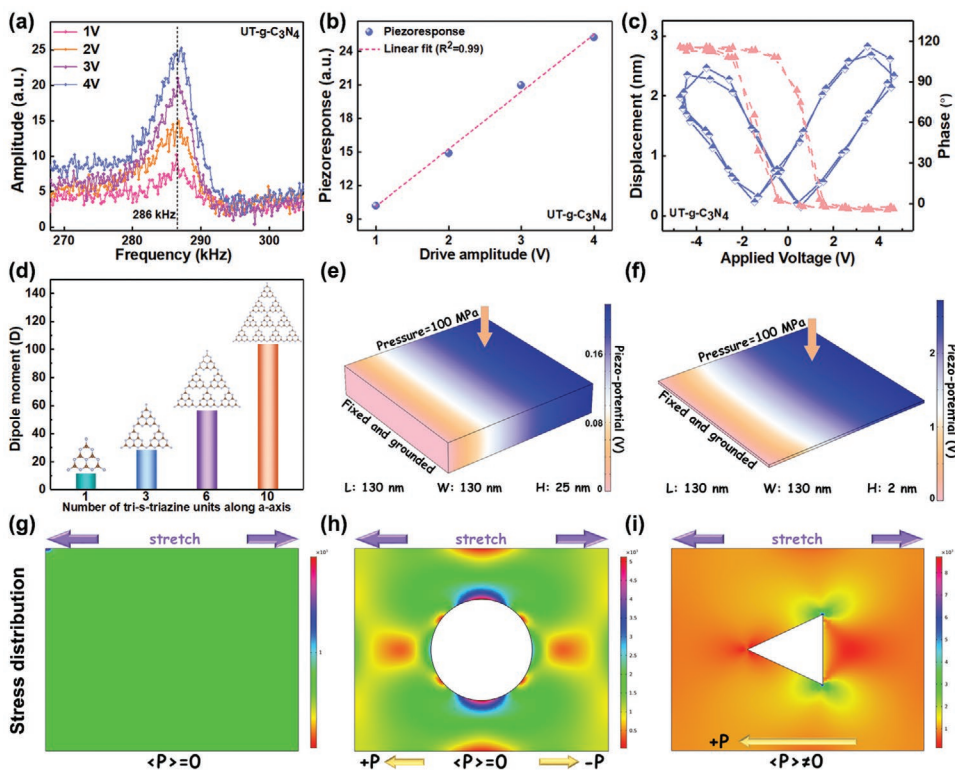


Figure 3. a) Resonant peaks for different applied voltages on UT- $\text{g-C}_3\text{N}_4$. b) Linear correlation between the operating voltage and the amplitude of UT- $\text{g-C}_3\text{N}_4$. c) The displacement–voltage curve and phase curve of UT- $\text{g-C}_3\text{N}_4$. d) The dipole moment of $\text{g-C}_3\text{N}_4$ monolayer with different numbers of tri-s-triazine units along the a -axis. e,f) FEM simulation for the piezoelectric potential distribution of bulk $\text{g-C}_3\text{N}_4$ (e) and UT- $\text{g-C}_3\text{N}_4$ (f) with the cavitation pressures of 100 MPa. g–i) FEM simulation for the stress distribution around the smooth plane (g), circular pore (h), and triangular pore (i) in tri-s-triazine sheets of $\text{g-C}_3\text{N}_4$.

is calculated by DFT. The single tri-s-triazine group exhibits a strong polarity with a dipole moment of 11.80 Debye (D) along the a -axis. With increasing the number of tri-s-triazine rings to 3, 6, and 10, the unit-cell net dipole moment along the a -axis is increased to 28.48, 56.35, and 103.69 D, respectively (Figure 3d). It manifests that the accumulation of polar tri-s-triazine units in the layer along the a -axis contributes to the strong in-plane polarization of $g\text{-C}_3\text{N}_4$. Hence, when the dipoles are stretched or compressed upon strain, the distance between the centers of positive and negative charges varies, inducing the in-plane piezoelectric response. Besides, the NCS triangular nanopores in tri-s-triazine sheets of $g\text{-C}_3\text{N}_4$ may generate strain gradients in the vicinity, which allows a nonzero net average polarization under mechanical vibration owing to the flexoelectric effect (Figure 3i). Nevertheless, the net polarization remains zero for the CS plane, though the strain gradients induced local polarization can be generated around the circular pore (Figure 3g,h). Consequently, the polar tri-s-triazine units and flexoelectric effect derived from the structured triangular nanopores collectively give rise to the strong in-plane polarization and the apparent piezoelectricity of $g\text{-C}_3\text{N}_4$ nanosheets. These polar layers are stacked in a graphite-like manner to form the bulk $g\text{-C}_3\text{N}_4$ so that the piezoelectricity is retained in bulk $g\text{-C}_3\text{N}_4$ (Figure S8, Supporting Information).

Though UT- $g\text{-C}_3\text{N}_4$ exhibits a larger piezoelectricity than bulk $g\text{-C}_3\text{N}_4$, the enhancement level (≈ 1.3 times) is not enough to contribute to the considerably promoted piezocatalysis

(≈ 3.1 times) and photo-piezocatalysis (≈ 3.5 times). Thus, the effects of morphology and thickness on the piezoelectric potential output are investigated via FEM. The piezo-potential difference of bulk $g\text{-C}_3\text{N}_4$ and $g\text{-C}_3\text{N}_4$ nanosheets under a sonication pressure of 100 MPa is theoretically calculated in Figure 3e,f. The much higher potential difference of $g\text{-C}_3\text{N}_4$ nanosheets (2.70 V) than bulk $g\text{-C}_3\text{N}_4$ (0.22 V) illustrates that the plate-like structure promotes the harvesting and conversion of mechanical energy (Figure S9, Supporting Information). Hence, the construction of ultrathin structures in $g\text{-C}_3\text{N}_4$ substantially facilitates the piezocatalytic process.

2.4. Mechanism of Photo-Enhanced Piezocatalysis

The improvement of photocatalytic performance by piezoelectric polarization has been extensively studied. However, the investigations on light-enhanced piezocatalysis are few. Herein, UT- $g\text{-C}_3\text{N}_4$ almost shows no H_2 evolution activity under illumination, though the photo-piezocatalytic process allows the highest yield of H_2 . In order to obtain an in-depth understanding on the photo-enhanced piezocatalytic process, KPFM is utilized to record the surface potential of samples under dark and illumination conditions (Figure S10, Supporting Information). As illustrated by Figure 4a–c, UT- $g\text{-C}_3\text{N}_4$ exhibits a surface potential of ≈ 16.4 mV under illumination, which decreases by ≈ 4.8 mV compared to that in the dark. The similar trend also appeared on the bulk $g\text{-C}_3\text{N}_4$, indicating that the piezo-induced

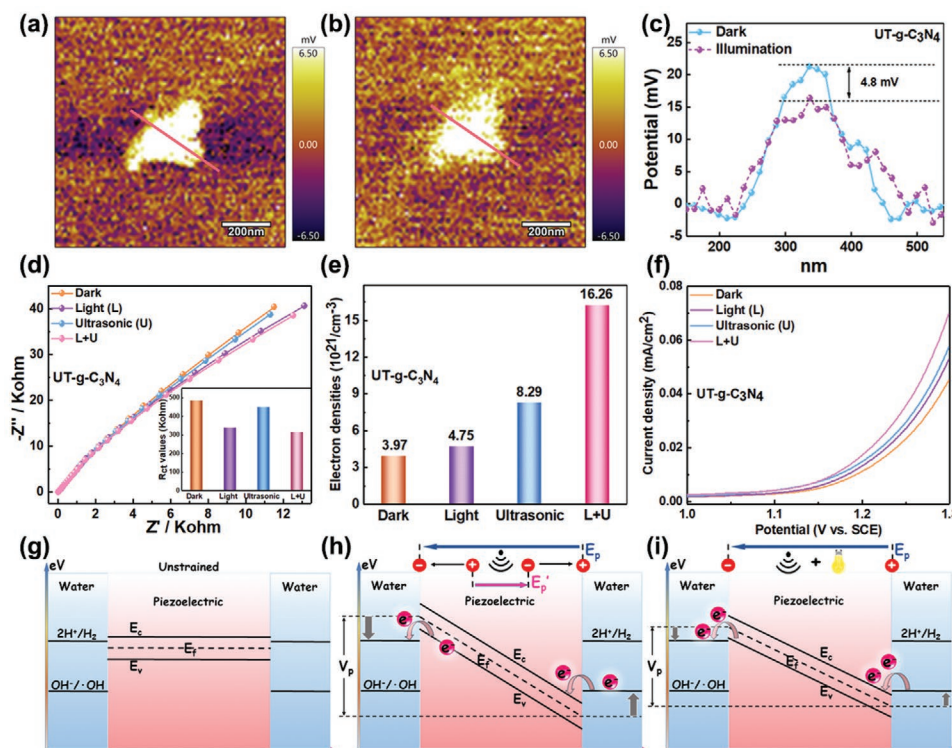


Figure 4. a, b) KPFM potential images of UT- $g\text{-C}_3\text{N}_4$ in the dark (a) and under illumination (b). c) The corresponding surface potential of UT- $g\text{-C}_3\text{N}_4$ measured in the dark and under illumination. d) EIS, e) the calculated charge density, and f) current density–voltage (I – V) curves of UT- $g\text{-C}_3\text{N}_4$ measured under different conditions. g–i) Schematic mechanism of the photo-improved piezocatalytic process.

polarization charges can be partially screened by the photo-generated carriers (Figures S11 and S12, Supporting Information). Hence, it can be concluded that the photoinduced electrons and holes are depleted by compensating polarization charges, and the residual piezoelectric charges participate in the surface redox reactions of the photo-piezocatalytic process. However, the reduced piezoelectric potential may result in the worse piezocatalytic activity under illumination, which is contrary to the present experimental results.

Theoretically, piezoelectricity-induced charges can be partially depleted to form the double layers for screening the piezoelectric potential near the interface, known as the capacitive current. While the other part of charges are consumed through charge transfer between the solution and piezoelectric surfaces, named as the Faradic current, and thus induce electrochemical reactions.^[50] Driven by the alternating mechanical vibration in the ultrasonic process, the direction of the induced piezoelectric electric field will change periodically, which results in the serious recombination of piezoelectric charges in a short time before forming capacitive and Faradic currents. Hence, the fast charge transfer between the piezoelectric and electroactive species is necessary for the available energized surface charges to fully take part in the reaction. Electrochemical impedance spectroscopy (EIS) measurement under different conditions is employed to illustrate the charge separation and transport in this process (Figure S13, Supporting Information). As shown in Figure 4d, the charge transfer resistance (R_{ct}) under simultaneous light and ultrasound is prominently reduced compared to that under ultrasound individually, demonstrating that the more efficient electron exchange between the piezoelectric charges and electroactive species is realized under illumination. The faster charge transfer allows more available piezoelectric charges for driving electrochemical reactions in the photo-piezocatalytic process. The highest current density obtained under the irradiation of light and ultrasound over UT-g-C₃N₄ further confirms the improved charge separation and transport in the piezocatalytic process by illumination (Figure 4f, Figure S14, Supporting Information).

In addition, the charge density under different conditions is determined by the Mott–Schottky measurement, according to the following formula:

$$N_d = \left(\frac{2}{e_0 \epsilon_0 \epsilon} \right) \left[d \frac{(1/C^2)}{dV} \right]^{-1} \quad (1)$$

where e_0 , ϵ_0 , and ϵ represent the electronic charge unit, the vacuum permittivity, and dielectric constant of g-C₃N₄, respectively.^[51] Under the condition of simultaneous light and ultrasound, UT-g-C₃N₄ demonstrates the smallest slope of Mott–Schottky plot, indicating the largest charge density. It is calculated to be $16.26 \times 10^{21} \text{ cm}^{-3}$, almost 2.0 times higher than under ultrasound and 3.4 times higher than that under light (Figure 4e). Combined with the above results, the photo-improved piezocatalytic process can be explicated in Figure 4g–i. A stable electrochemical equilibrium between the piezoelectric and solution is arrived without the stress applied. Under stress, the deformed piezoelectric suffers from

an energy shift on the CB and VB across the material and produces a piezo-potential (V_p), which drives the flow of electrons from the VB of piezoelectric to species in solution for H₂ evolution at the negatively charged end. Meanwhile, water oxidation occurs on the positive side with a net electron flow transferring into the CB of the piezocatalyst. Nevertheless, the ultrasound-induced alternate piezoelectric field (E_p) results in the recombination of piezoelectric charges before reactions, restricting the piezocatalytic performance of g-C₃N₄. With the simultaneous light and ultrasound, the improved electron exchange between the piezoelectric charges and electroactive species allows more available energized surface charges to reduce/oxidize water before the occurrence of an opposite direction E_p , even though the charge-induced potential amplitude decreased. Hence, it can be concluded that the fast charge transfer and moderate energy shift is critical for the kinetics of light-enhanced piezocatalytic H₂ production.

It has been reported that the unsatisfied catalytic activity of g-C₃N₄ is mainly attributable to the insufficient active sites on the surface.^[52] To get an in-depth insight into the high piezocatalytic and photo-piezocatalytic H₂ evolution performance and the catalytic activity difference of UT-g-C₃N₄ under different conditions, the reductive reactive sites are investigated by depositing Ag nanoparticles with different irradiation sources (Figure 5b). As shown in Figure S15 (Supporting Information), almost no Ag nanoparticles are deposited on the UT-g-C₃N₄ under visible light irradiation, indicating the poor photocatalytic activity. With ultrasonic irradiation, some Ag nanoparticles are obviously deposited on the edges of the nanosheets, suggesting that the strain-induced q^- reduces the adsorbed Ag⁺ at the marginal active sites due to the piezoelectric polarization along the tri-s-triazine plane, which has been verified by DFT (Figure 5a). To probe structural change in the piezocatalysis, in situ high pressure is exerted on UT-g-C₃N₄ nanosheets to simulate this process, and Raman spectroscopy is measured under different pressures. Obviously, the strong peak at 705 cm⁻¹ gradually shifts toward higher wavenumber with increasing the pressure from 0 to 0.5 GPa, which reveals the existence of defects in the framework of g-C₃N₄ (Figure 5d). It has been reported that the formation energy of nitrogen and carbon vacancies in g-C₃N₄ nanosheets is decreased to 1.05 and 0.1 eV at -2% of compressive strain, respectively, indicating the carbon vacancies are more easily formed upon cavitation pressure.^[53,54] Thus, the strain-induced carbon vacancies can serve as the active sites to facilitate the adsorption and activation of reactants, resulting in the favorable piezocatalytic activity of UT-g-C₃N₄. Due to the chaotic direction of ultrasonic vibration applied to the nanosheets, it can be speculated that the strain-induced vacancies should exist across the nanosheets, not just on the edges. Interestingly, Ag nanoparticles are found to appear at the both edges and basal planes of nanosheets under simultaneous light and ultrasound. It should be ascribed to the fast charge transport for enriching the reactive sites, which facilitates the activation of Ag⁺ adsorbed at the planar active sites (Figure 5c). Hence, the photo-improved surface charge transfer and strain-enriched surface reactive sites collectively lead to the preferable H₂ production performance of UT-g-C₃N₄ by the photo-piezocatalytic process (Figure 5e).

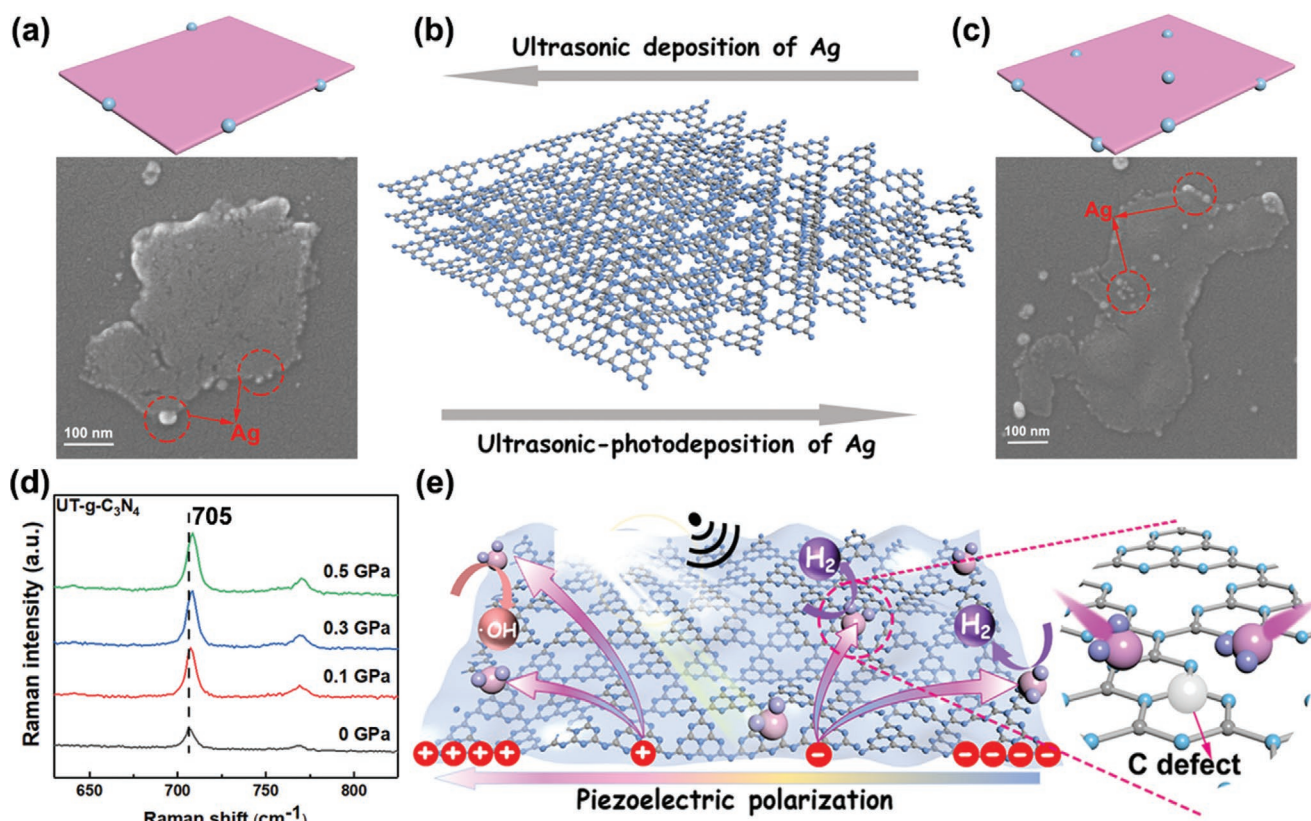


Figure 5. a, c) Deposition of Ag nanoparticles on UT-g-C₃N₄ nanosheets under ultrasound (a) and simultaneous light and ultrasound (c). b) Schematic diagram of the Ag deposition experiments. d) In situ high-pressure Raman spectra of UT-g-C₃N₄ under gradient stress. e) Schematic illustration of the photo-piezocatalytic process over UT-g-C₃N₄.

3. Conclusion

Ultrathin g-C₃N₄ nanosheets are prepared by combined direct thermal oxidation etching and ultrasonic exfoliation from bulk g-C₃N₄. Under the co-irradiation of light and ultrasound, UT-g-C₃N₄ exhibits a superb photo-piezocatalytic H₂ evolution rate of 12.16 mmol g⁻¹ h⁻¹ without any cocatalysts loaded, and still maintains a high activity (8.97 mmol g⁻¹ h⁻¹) in the pure-water-splitting reaction with production of value-added H₂O₂ as oxidation product. It outperforms the reported piezocatalysts and g-C₃N₄-based photocatalysts under the similar conditions. DFT calculations and FEM simulations disclose that the preferable piezoelectricity of g-C₃N₄ nanosheets is derived from the in-plane polarization induced by the additive dipole moment of polar tri-s-triazine units and flexoelectric effect. In situ high-pressure Raman spectroscopy and electrochemical characterizations with different irradiation sources uncover that the enriched surface reactive sites by the strain-created carbon vacancies and improved charge exchange between the piezoelectric and electroactive species by illumination facilitate the reaction kinetics of water splitting. The above advantages collectively contribute to the outstanding photo-piezocatalytic H₂ evolution performance of ultrathin g-C₃N₄ nanosheets. This study provides a novel and efficient route to utilize mechanical and solar energy for H₂ production, and opens the gate of developing g-C₃N₄-based polar semiconductors as the high-performance photo-piezocatalysts.

Supporting Information

Supporting Information is available from the Wiley Online Library or from the author.

Acknowledgements

This work was jointly supported by the National Natural Science Foundation of China (Nos. 51972288 and 51672258) and the Fundamental Research Funds for the Central Universities (2652018287).

Conflict of Interest

The authors declare no conflict of interest.

Data Availability Statement

Research data are not shared.

Keywords

charge transport, hydrogen evolution, photo-piezocatalysis, reactive sites

Received: March 4, 2021
Revised: March 20, 2021
Published online: May 8, 2021

- [1] X. Chen, S. Shen, L. Guo, S. S. Mao, *Chem. Rev.* **2010**, *110*, 6503.
- [2] W. Lubitz, W. Tumas, *Chem. Rev.* **2007**, *107*, 3900.
- [3] M. Z. Rahman, M. G. Kibria, C. B. Mullins, *Chem. Soc. Rev.* **2020**, *49*, 1887.
- [4] S. Wang, X. Han, Y. Zhang, N. Tian, T. Ma, H. Huang, *Small Struct.* **2021**, *2*, 2000061.
- [5] M. Wang, Y. Zuo, J. Wang, Y. Wang, X. Shen, B. Qiu, L. Cai, F. Zhou, S. P. Lau, Y. Chai, *Adv. Energy Mater.* **2019**, *9*, 1901801.
- [6] F. Chen, T. Ma, T. Zhang, Y. Zhang, H. Huang, *Adv. Mater.* **2021**, *33*, 2005256.
- [7] C. Hu, S. Tu, N. Tian, T. Ma, Y. Zhang, H. Huang, *Angew. Chem., Int. Ed.* **2021**, <https://doi.org/10.1002/anie.202009518>.
- [8] L. Pan, S. Sun, Y. Chen, P. Wang, J. Wang, X. Zhang, J.-J. Zou, Z. L. Wang, *Adv. Energy Mater.* **2020**, *10*, 2000214.
- [9] Q. Yang, X. Guo, W. Wang, Y. Zhang, S. Xu, D. H. Lien, Z. L. Wang, *ACS Nano* **2010**, *4*, 6285.
- [10] C. Tan, X. Cao, X.-J. Wu, Q. He, J. Yang, X. Zhang, J. Chen, W. Zhao, S. Han, G.-H. Nam, M. Sindoro, H. Zhang, *Chem. Rev.* **2017**, *117*, 6225.
- [11] Y. Sun, S. Gao, F. Lei, Y. Xie, *Chem. Soc. Rev.* **2015**, *44*, 623.
- [12] J. Tan, S. Li, B. Liu, H.-M. Cheng, *Small Struct.* **2021**, *2*, 2000093.
- [13] J. Yang, W. Li, D. Wang, Y. Li, *Small Struct.* **2021**, *2*, 2000051.
- [14] W. Feng, J. Yuan, L. Zhang, W. Hu, Z. Wu, X. Wang, X. Huang, P. Liu, S. Zhang, *Appl. Catal., B* **2020**, *277*, 119250.
- [15] J. M. Wu, W. E. Chang, Y. T. Chang, C.-K. Chang, *Adv. Mater.* **2016**, *28*, 3718.
- [16] Y. Su, L. Zhang, W. Wang, X. Li, Y. Zhang, D. Shao, *J. Mater. Chem. A* **2018**, *6*, 11909.
- [17] W. Feng, J. Yuan, F. Gao, B. Weng, W. Hu, Y. Lei, X. Huang, L. Yang, J. Shen, D. Xu, X. Zhang, P. Liu, S. Zhang, *Nano Energy* **2020**, *75*, 104990.
- [18] N. Tian, H. Huang, X. Du, F. Dong, Y. Zhang, *J. Mater. Chem. A* **2019**, *7*, 11584.
- [19] N. Tian, H. Huang, S. Wang, T. Zhang, X. Du, Y. Zhang, *Appl. Catal., B* **2020**, *267*, 118697.
- [20] S. Chandratre, P. Sharma, *Appl. Phys. Lett.* **2012**, *100*, 023114.
- [21] M. Zelisko, Y. Hanlumuayang, S. Yang, Y. Liu, C. Lei, J. Li, P. M. Ajayan, P. Sharma, *Nat. Commun.* **2014**, *5*, 4284.
- [22] R.-C. Wang, Y.-C. Lin, H.-C. Chen, W.-Y. Lin, *Nano Energy* **2021**, *83*, 105743.
- [23] K. Wang, D. Shao, L. Zhang, Y. Zhou, H. Wang, W. Wang, *J. Mater. Chem. A* **2019**, *7*, 20383.
- [24] P. Niu, L. Zhang, G. Liu, H.-M. Cheng, *Adv. Funct. Mater.* **2012**, *22*, 4763.
- [25] H. Huang, K. Xiao, N. Tian, F. Dong, T. Zhang, X. Du, Y. Zhang, *J. Mater. Chem. A* **2017**, *5*, 17452.
- [26] J. Jiang, L. Ou-yang, L. Zhu, A. Zheng, J. Zou, X. Yi, H. Tang, *Carbon* **2014**, *80*, 213.
- [27] Y. Li, R. Jin, Y. Xing, J. Li, S. Song, X. Liu, M. Li, R. Jin, *Adv. Energy Mater.* **2016**, *6*, 1601273.
- [28] C. Hu, H. Huang, F. Chen, Y. Zhang, H. Yu, T. Ma, *Adv. Funct. Mater.* **2020**, *30*, 1908168.
- [29] Y. Hou, A. B. Laursen, J. Zhang, G. Zhang, Y. Zhu, X. Wang, S. Dahl, I. Chorkendorff, *Angew. Chem., Int. Ed.* **2013**, *52*, 3621.
- [30] J. Hong, Y. Wang, Y. Wang, W. Zhang, R. Xu, *ChemSusChem* **2013**, *6*, 2263.
- [31] J. Yu, S. Wang, B. Cheng, Z. Lin, F. Huang, *Catal. Sci. Technol.* **2013**, *3*, 1782.
- [32] W. Zhou, T. Jia, D. Zhang, Z. Zheng, W. Hong, X. Chen, *Appl. Catal., B* **2019**, *259*, 118067.
- [33] M. S. Nasir, G. Yang, I. Ayub, S. Wang, W. Yan, *Appl. Catal., B* **2020**, *270*, 118900.
- [34] C. Liu, H. Huang, L. Ye, S. Yu, N. Tian, X. Du, T. Zhang, Y. Zhang, *Nano Energy* **2017**, *41*, 738.
- [35] Q. Liu, J. Shen, X. Yu, X. Yang, W. Liu, J. Yang, H. Tang, H. Xu, H. Li, Y. Li, J. Xu, *Appl. Catal., B* **2019**, *248*, 84.
- [36] Q. Han, B. Wang, J. Gao, Z. Cheng, Y. Zhao, Z. Zhang, L. Qu, *ACS Nano* **2016**, *10*, 2745.
- [37] Y.-P. Zhu, T.-Z. Ren, Z.-Y. Yuan, *ACS Appl. Mater. Interfaces* **2015**, *7*, 16850.
- [38] N. Tian, Y. Zhang, X. Li, K. Xiao, X. Du, F. Dong, G. I. N. Waterhouse, T. Zhang, H. Huang, *Nano Energy* **2017**, *38*, 72.
- [39] J. Liu, W. Fang, Z. Wei, Z. Qin, Z. Jiang, W. Shangguan, *Appl. Catal., B* **2018**, *238*, 465.
- [40] Q. Han, B. Wang, Y. Zhao, C. Hu, L. Qu, *Angew. Chem., Int. Ed.* **2015**, *54*, 11433.
- [41] B. Lin, H. An, X. Yan, T. Zhang, J. Wei, G. Yang, *Appl. Catal., B* **2017**, *210*, 173.
- [42] L. Ma, H. Fan, K. Fu, S. Lei, Q. Hu, H. Huang, G. He, *ACS Sustainable Chem. Eng.* **2017**, *5*, 7093.
- [43] B. Lin, G. Yang, L. Wang, *Angew. Chem., Int. Ed.* **2019**, *58*, 4587.
- [44] J. Yuan, X. Liu, Y. Tang, Y. Zeng, L. Wang, S. Zhang, T. Cai, Y. Liu, S. Luo, Y. Pei, C. Liu, *Appl. Catal., B* **2018**, *237*, 24.
- [45] Y. Yu, W. Yan, X. Wang, P. Li, W. Gao, H. Zou, S. Wu, K. Ding, *Adv. Mater.* **2018**, *30*, 1705060.
- [46] X. Xu, L. Xiao, Z. Wu, Y. Jia, X. Ye, F. Wang, B. Yuan, Y. Yu, H. Huang, G. Zou, *Nano Energy* **2020**, *78*, 105351.
- [47] H. You, Z. Wu, L. Zhang, Y. Ying, Y. Liu, L. Fei, X. Chen, Y. Jia, Y. Wang, F. Wang, S. Ju, J. Qiao, C.-H. Lam, H. Huang, *Angew. Chem., Int. Ed.* **2019**, *58*, 11779.
- [48] Y.-C. Wang, J. M. Wu, *Adv. Funct. Mater.* **2020**, *30*, 1907619.
- [49] R. Su, H. A. Hsain, M. Wu, D. Zhang, X. Hu, Z. Wang, X. Wang, F.-t. Li, X. Chen, L. Zhu, Y. Yang, Y. Yang, X. Lou, S. J. Pennycook, *Angew. Chem., Int. Ed.* **2019**, *58*, 15076.
- [50] M. B. Starr, J. Shi, X. Wang, *Angew. Chem., Int. Ed.* **2012**, *51*, 5962.
- [51] S. Zhang, Z. Liu, M. Ruan, Z. Guo, L. E. W. Zhao, D. Zhao, X. Wu, D. Chen, *Appl. Catal., B* **2020**, *262*, 118279.
- [52] X. Dong, F. Cheng, *J. Mater. Chem. A* **2015**, *3*, 23642.
- [53] J. Ding, W. Xu, H. Wan, D. Yuan, C. Chen, L. Wang, G. Guan, W.-L. Dai, *Appl. Catal., B* **2018**, *221*, 626.
- [54] X. Liu, W. Kang, W. Zeng, Y. Zhang, L. Qi, F. Ling, L. Fang, Q. Chen, M. Zhou, *Appl. Surf. Sci.* **2020**, *499*, 143994.